Anisoplanatic imaging through turbulence using principal component analysis

Roberto Baena-Gallé
Real Academia de Ciencias y Artes de Barcelona

Szymon Gladysz
Fraunhofer Institute of Optronics,
System Technologies and Image Exploitation IOSB

Javier Mateos
Universidad de Granada

ABSTRACT

The performance of optical systems is highly degraded by atmospheric turbulence when observing both vertically (e.g., astronomy, remote sensing) or horizontally (e.g. long-range surveillance). This problem can be partially alleviated using adaptive optics (AO) but only for small fields of view (FOV), described by the isoplanatic angle, for which the turbulence-induced aberrations can be considered constant. Additionally, this problem can also be tackled using post-processing techniques such as deconvolution algorithms which take into account the variability of the point spread function (PSF) in anisoplanatic conditions.

Variability of the PSF across the field of view in anisoplanatic imagery can be described using principal component analysis. Then, a certain number of variable PSFs can be used to create new basis functions, called principal components (PC), which can be considered constant across the FOV and, therefore, potentially be used to perform global deconvolution. Our approach is tested on simulated, single-conjugate AO data.

1. INTRODUCTION

Deconvolution algorithms almost always assume a constant PSF across the degraded image. This simplification allows to perform deconvolution operations over the entire field of view (FOV) using e.g. the fast Fourier transform (FFT), thus reducing the computational cost. However, there are many situations where the assumption of spatial invariance is not valid. For instance, camera shake, object motion, optical aberrations or atmospheric turbulence are typical cases where the PSF can vary significantly across FOV [1].

Atmospheric turbulence is one the most important factors that degrade the quality of an image in astronomical observations, remote sensing or long-range surveillance and reconnaissance. This reduction of quality can be partially corrected by means of adaptive optics (AO) but only within the so-called isoplanatic angle. When the FOV is much larger than this angle the variability of the PSF becomes visible. Fig. 1 shows a simulated long exposure image of a stellar field observed with the 3.5-m Starfire Optical Range (SOR) telescope (details of the simulation are described in Section 4). The AO guide star (GS) has been placed in the center of the FOV. The reader should note how the PSF elongation becomes more important for the stars located further out from the GS.

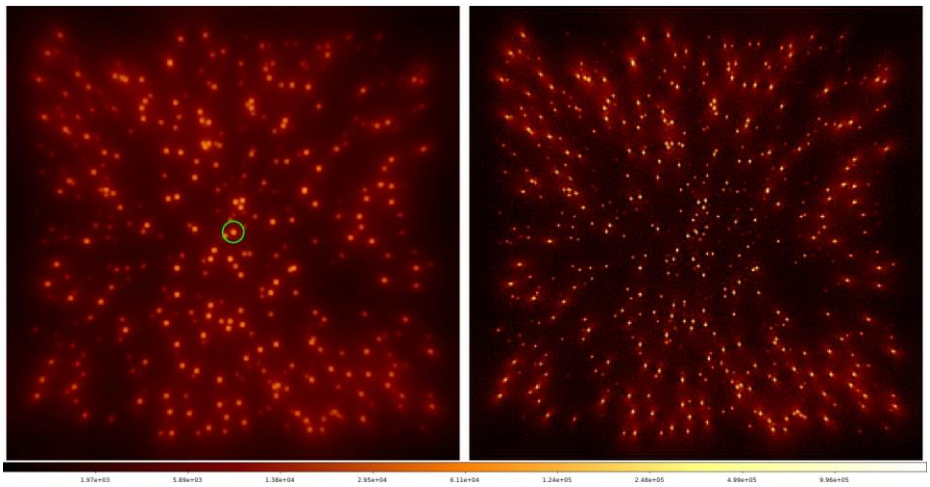

Fig. 1. Left: anisoplanatic AO simulation with the 3.5-m SOR telescope for atmosphere 1 (details of the simulation can be found in Section 4). Location of the GS is marked with a green circle. Right: Richardson-Lucy deconvolution using the GS as reference PSF. Image are shown in log scale and in false colors.

A typical way to deal with this situation is to divide the image into small non-overlapping regions where the PSF can be assumed constant, then perform local deconvolution and stitch all pieces back together again. Larger, partially-overlapping regions can be used to reduce artifacts at the boundaries by interpolating the influences of the different PSFs in the common regions [2].

A more elegant method consists in representing the varying set of PSFs through an appropriate basis. Then, the PSFs are expressed as weighted sums of functions whereby each of these functions can be assumed to be spatially invariant. Representing a PSF as a linear combination of functions is not a new idea. For instance, the wavelet transform (WT) provides a set of fast-decaying functions that decompose the frequency content of a signal, spatially localizing such content simultaneously. Since PSFs are in general sharp and compact, the WT can be used to represent their variability [3]. The shapelet transform (ST) also offers a highly localized orthogonal set, which is derived from Gaussian-weighted Hermite polynomials. It was proposed to represent astronomical objects, in particular, weak gravitational lensing phenomena [4]. Unfortunately, neither of them is able to represent correctly at the same time all the possible features at small and large scales [5].

Unlike WT and ST, principal component analysis (PCA) is not based on common analytical functions but on the data itself, thus increasing its efficiency in the representation of the data. In a nutshell, the derived functions are the eigenvectors of the covariance matrix created from the data to be represented. In reference [6] the authors use filter banks computed through PCA to convolve raw images for representing different types of blurring, such as foveal vision or aberrations experienced by a glaucoma patient, among others. The use of PCA allows for choosing an informed trade-off between accuracy of the representation and computational cost.

To our knowledge, reference [7] was the first to propose the use of PCA in the deconvolution operation to account for the variability of PSFs in AO observations. The authors show that the spatially-varying deconvolution problem can be tackled by a weighted sum of a series of spatially-invariant deconvolutions. The chosen algorithm for spatially-invariant deconvolution was the Richardson-Lucy (RL) method, which obtains the maximum likelihood solution in the presence of Poisson noise. Reference [7] shows the performance of this approach on images acquired with the QUIRC/Hokupa'a AO instrument.

Reference [8] presents a myopic algorithm that also assumes Poisson noise in the data fidelity term. The anisoplanatism of the PSFs is described with one parameter that modifies the turbulence power spectral density based on the von Karman model. In particular, it linearly modifies the layer altitudes of a proposed atmosphere profile, thus stretching or compressing its structure while preserving its morphology. In practice, this means keeping constant the set of functions and scaling the coefficients that weight them by a factor which must be estimated during the minimization process, thus justifying the myopic nature of this approach.

Reference [9] introduces PCA in the L0-AbS algorithm, short for l_0 analysis-based sparsity. This is an iterative, regularized filter that assumes Gaussian noise for the likelihood and a l_0-based prior for the object. A threshold is applied to the solution at each iteration using a combination of the 2-D dual tree complex wavelet transform and the translation-invariant Haar pyramid. This approach shows good results for different types of extended objects.

The goal of this paper is to test PCA on simulated PSFs from the single-conjugate AO system at SOR. Two deconvolution algorithms were modified to include PCA. The influence of the number of principal components on the subsequent global image reconstruction was tested. The comparison of this approach vs. traditional deconvolution with a single PSF was also carried out.

This paper is organized as follows. In Section 2 the technique of decomposing a dataset in its principal components (PC) is described. Section 3 is intended to show how to include PCs into some iterative deconvolution algorithms. Section 4 describes the AO simulations used in this work and the obtained results. Finally, Section 5 outlines future directions.

2. SPATIALLY VARIANT CONVOLUTION USING PCA

The observed image $i(\vec{x})$ is given by the standard image formation equation, which expresses the image at a position $\vec{x}$ as the convolution of an object $o(\vec{u})$ with a PSF $h(\vec{u},\vec{x})$ that accounts for distortions caused by atmospheric turbulence, relative camera motion or optical aberrations:

$$i(\vec{x}) = o(\vec{u}) \otimes h(\vec{u},\vec{x}) + n(\vec{x}) \tag{1}$$

where $\otimes$ denotes the convolution operator, $n(\vec{x})$ accounts for the noise from the source and the detector, and $\vec{x}$ and $\vec{u}$ are 2-D vectors denoting image-, and object-space coordinates, respectively. Note that the PSF is assumed to change with $\vec{u}$ and $\vec{x}$. If the PSF can be approximated as a weighted sum of J functions (hereafter we use the term eigen-PSF or principal component -PC- to denote such functions):

$$h(\vec{u},\vec{x}) \approx \sum_{j=1}^{J} a_j(\vec{u}) \cdot h_j(\vec{x}) \tag{2}$$

then Equation (1) becomes:

$$i(\vec{x}) \approx \sum_{j=1}^{J} \left[(a_j \cdot o) \otimes h_j \right](\vec{x}) + n(\vec{x}) \tag{3}$$

The set of h_j's forms a basis of space-invariant PSFs that can be convolved independently with the object, and whose influence/weighting over the object is determined by the set of coefficients a_j. In other words, a_j's weight the object domain according to the variability expressed by the h_j's. To compute both h_j's and a_j's an appropriate basis must be chosen. Principal component analysis (PCA) creates an orthogonal basis such that the first eigen-PSF accounts for as much of the variability present in the data as possible, and each succeeding eigen-PSF has the highest variance possible under the constraint to be orthogonal to the preceding eigen-PSF.

The way to compute PCA in order to find the elements of the decomposition in Equation (2) is by means of singular value decomposition (SVD) [10], for which the PSF $h(\vec{u},\vec{x})$ must be arranged into a matrix K that is built in the following way. Let us consider an $M \times M$ pixel FOV representing an extended object or a stellar field. As an example suppose that $M = 256$ so the total number of pixels in the FOV is 65536. At each location or pixel there is a representation of a space-variant PSF. If the support of the PSFs is $N \times N$ pixels, and for example $N = 64$, then one needs a total number of M^2 vectors of N^2 size (lexicographically-ordered PSFs), i.e., 65536 vectors of size 4096 that represent the total PSF variability in the FOV. Hence, K is a $M^2 \times N^2$ matrix with as many columns as PSFs and as many rows as individual PSF elements. Singular value decomposition of matrix K results in:

$$K = U \Lambda V^T \tag{4}$$

where U and V are two matrices with orthonormal columns containing the eigen-PSFs h_j's and coefficients a_j's, respectively, and Λ is a diagonal matrix whose elements are the eigenvalues of the decomposition. At this point it is important to stress that every PSF should be centered so that the peak always lies at the center pixel of the PSF support, otherwise, the SVD would be dominated by PSF translation rather than by its shape. The maximum number of useful eigen-PSFs will be limited by the rank of matrix K, i.e., the lowest of the two numbers: M^2 or N^2. In our work $M \gg N$, and so we will obtain a maximum number of N^2 eigen-PSFs (4096, using the numbers quoted above). In order to reduce the dimensionality of the problem it is preferable to work with the covariance matrix of K rather than with K itself, thus results a symmetric $N^2 \times N^2$ matrix. Singular value decomposition of this covariance matrix can be expressed as:

$$Cov(K) = KK^T = U\Lambda V^T V\Lambda^{\mathrm{T}}\mathrm{U}^{\mathrm{T}} = \mathrm{U}\Lambda^2\mathrm{U}^{\mathrm{T}} \tag{5}$$

Each of the eigen-PSFs h_j, which forms the orthonormal basis we are interested in, can be obtained from the columns of the matrix U. The field of coefficients a_j's can be obtained directly from the rows of $U^T K$. The value of the corresponding eigenvalue in the matrix Λ gives the importance of its eigenvector. The larger the eigenvalue, the more variability is contained in the corresponding eigen-PSF. Notice that since we assume we have access to the PSFs at all locations, then we will be able to compute all the coefficients at each of these locations for each eigen-PSF, otherwise one would have to interpolate a_j's to obtain those coefficients where the PSF is unknown [11].

Exact recovery of the original PSFs requires the use of all possible eigen-PSFs that can be obtained from PCA. However, if only the first J eigen-PSFs are kept, then the recovered data has the maximum possible variance that could be preserved from the original data whereas the square reconstruction error is minimum. This characteristic allows PCA to retain as much of the original variance as possible with only a few eigen-PSFs, thus reducing the computational overhead associated with Equation (3).

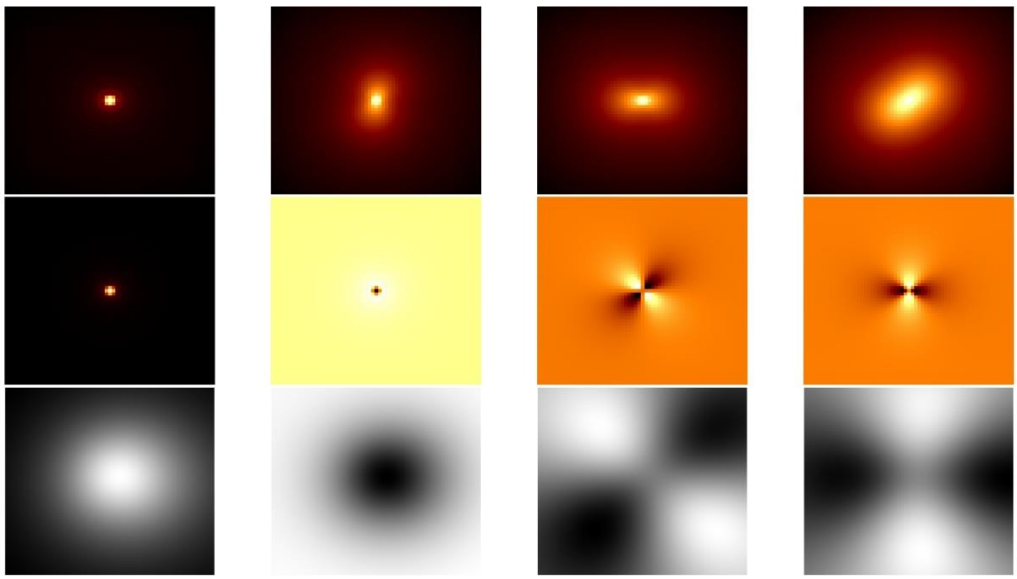

Fig. 2. First row: example simulated PSFs from positions (127,127), (1,127), (127,1) and (1,1) respectively, within a FOV of 256×256 pixels. The support of these PSFs is 64×64 pixels. Second row: first four eigen-PSFs shown from left to right in order of decreasing importance according to their respective eigenvalues. The support of these eigen-PSFs is also 64×64 pixels. Third row: coefficient fields associated with the corresponding eigen-PSFs above. The support of the coefficient field is the same as the FOV, i.e., 256×256 pixels.

Fig. 2 shows the result of PCA over PSFs within a 256×256 FOV (see Section 4 for description of the input data). Notice how the first two eigen-PSFs are related to the size of the original PSFs, while the next two describe the elongations along the diagonals and horizontal-vertical directions, respectively. The coefficients weight the importance of an eigen-PSF to obtain the correct PSF at each location. For example, the sign of the coefficient in

the third row, fourth column determines whether the associated eigen-PSF will be elongated in the horizontal or vertical direction at a given location in the FOV (second row, fourth column). In our study we have knowledge of PSFs at every location and so we can compute the entire fields of coefficients, otherwise there would be missing points in the third row in Fig. 2.

The importance of each eigen-PSF is expressed by its corresponding eigenvalue. The larger the eigenvalue the more information is contained in the eigen-PSF. Table 1 and Fig. 3 quantify the importance of the first 10 eigen-PSFs. The first 4 eigen-PSFs (Fig. 2, second row) contain more than 95% of the original information, 99% is contained in the first 10 eigen-PSFs. If the PSF support is 64×64 pixels then it is possible to produce a total number of 4096 eigen-PSFs. Although all of them are necessary to recover the original PSFs exactly, only a few of them are needed to obtain a relatively close recovery. This implies an important reduction in the computational cost needed to deal with the problem.

Table 1. Example PCA analysis based on atmosphere 2 from simulation described in Section 4. Variation is defined as the percentage a particular eigenvalue forms with respect to the sum of all the eigenvalues.

Eigen-PSF no.	Eigenvalue	Variation (%)	Accumulated Variation (%)
1	16,29	69,75	69,75
2	3,91	16,73	86,48
3	1,15	4,91	91,39
4	1,03	4,40	95,79
5	0,33	1,43	97,22
6	0,15	0,63	97,85
7	0,10	0,44	98,29
8	0,09	0,38	98,67
9	0,05	0,22	98,89
10	0,04	0,17	99,06

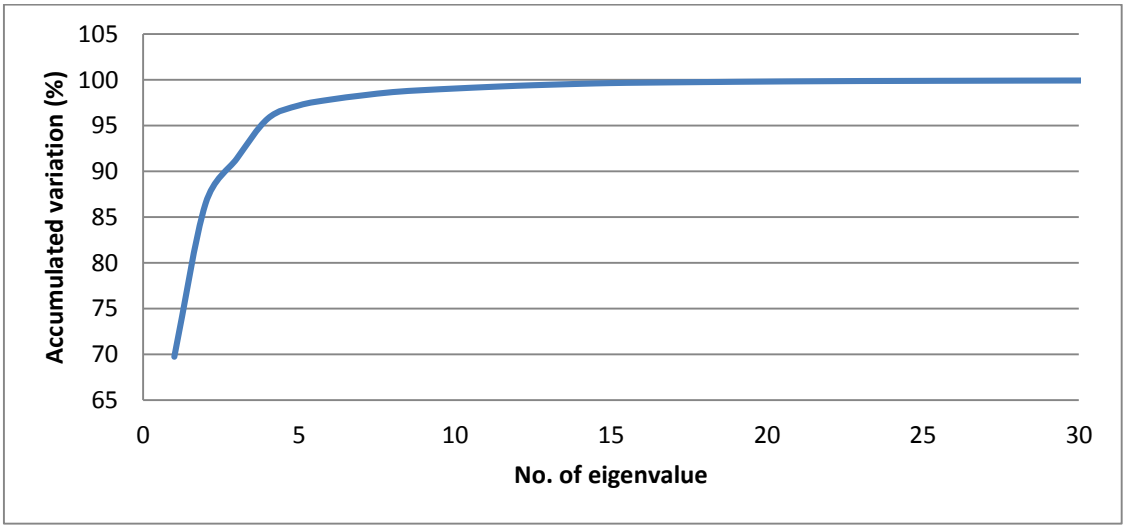

Fig. 3. Accumulated variation per eigen-PSF. Only 4 eigen-PSFs (second row in Fig. 2) are enough to represent 95% of the total variability present in the original 65536 PSFs. With 10 eigen-PSFs it is possible to represent more than 99% of the PSF variability in the FOV.

3. DECONVOLUTION ALGORITHMS WITH PCA

Inclusion of PCA into deconvolution algorithms is relatively easy. In particular, with respect to the Richardson-Lucy (RL) method [7], it basically consists in substituting the expression for $h(\vec{u},\vec{x})$ by the weighted sum $\sum_{j=1}^{J} a_j(\vec{u})h_j(\vec{x})$, J being the desired number of considered eigen-PSFs. The equation for RL iteration is as follows:

$$o^{(n+1)} = \left[h^T \otimes \left(\frac{i}{h \otimes o^{(n)}}\right)\right]^{\gamma} \cdot o^{(n)} \tag{6}$$

where n is iteration number, γ is a parameter that speeds up the convergence rate when $\gamma > 1$ and slows it down when $\gamma < 1$, and h^T is the conjugate of the Fourier transform of the PSF or its 180° rotated version in the spatial domain. With PCA, Equation (6) is modified in the following manner:

$$o^{(n+1)} = \left[\sum_{j=1}^{J}\left(h_j^T \otimes \left(\frac{i}{\sum_{j=1}^{J} h_j \otimes (a_j \cdot o^{(n)})}\right)\right) \cdot a_j\right]^{\gamma} \cdot o^{(n)} \tag{7}$$

The current estimate for the object at iteration n must be weighted by the corresponding set of coefficients a_i associated with the eigen-PSFs h_j. The result is convolved with the eigen-PSFs (and added up) and compared with the dataset i. This correcting term is then convolved again with the set of rotated eigen-PSFs h_j^T and coefficients a_j in order to express it in the object space, before its multiplication with the current estimate. Notice that h_j^T still uses the same set of a_j's.

In the same way PCA can be applied to the Landweber method [12] which yields the maximum likelihood solution in the presence of Gaussian noise, instead of Poisson noise as RL does. Such approach results in the following iterative method:

$$o^{(n+1)} = \left[\sum_{j=1}^{J}\left(h_j^T \otimes \left(i - \sum_{j=1}^{J} h_j \otimes \left(a_j \cdot o^{(n)}\right)\right)\right) \cdot a_j\right]^{\gamma} + o^{(n)} \tag{8}$$

In a similar way, reference [9] modifies the L0-AbS algorithm which is a regularized inverse filter that assumes Gaussian statistics for the likelihood term. Its iteration can be expressed in the Fourier domain as:

$$O^{(n+1)} = \frac{O_t^{(n)} + \upsilon \cdot H^* \cdot I}{1 + \upsilon \cdot |H|^2} \tag{9}$$

Capital letters denote Fourier transformation and $O_t^{(n)}$ is a filtered version of the current estimate after thresholding in the wavelet domain using the 2-D dual tree complex WT or the translation-invariant Haar pyramid (or a combination of both). The wavelet coefficients are modeled as a strictly sparse vector following an l_0 norm approach with a rate parameter α plus a white and Gaussian residual term of standard deviation σ_r. Both model parameters α and σ_r must be chosen by the user. Regularization parameter υ depends on σ_r and the noise level.

To compute Equation (9) using PCA, reference [9] proposes to decouple the problem, i.e., for a certain value of the regularization parameter υ, both the set of original PSFs $h(\vec{u},\vec{x})$ and the set of derived filters $f(\vec{u},\vec{x}) = \mathcal{F}^{-1}\left(\frac{1}{1+\upsilon \cdot |H|^2}\right)$ obtained from the PSFs, are decomposed with PCA independently. Hence, one applies SVD twice, the first time to obtain $h(\vec{u},\vec{x}) = \sum_{j=1}^{J} a_j(\vec{u}) \cdot h_j(\vec{x})$ and the second time to obtain $f(\vec{u},\vec{x}) = \sum_{j=1}^{J} b_j(\vec{u}) \cdot f_j(\vec{x})$.

Principal components of the PSFs will be applied in the numerator of Equation (9) and PCs of the derived filters will be applied to the resulting term. If it is possible to assume that both $h(\vec{u},\vec{x})$ and $f(\vec{u},\vec{x})$ change smoothly across the FOV, then this double decomposition will provide an approximation close enough to the exact solution [9]. Furthermore, it should be noted that both PC decompositions must be computed only once for all the iterations of the algorithm, and not for every iteration again.

4. DATA DESCRIPTION AND RESULTS

In the scope of the current work it is assumed that PCA and the deconvolution algorithm can be supplied with PSFs for every location in the FOV. How this very detailed information about anisoplanatism could be obtained in practice remains an open question but at this stage the main goal is to determine the benefits of treating anisoplanatism rigorously through PCA as opposed to simply ignoring the problem and deconvolving the whole image at once with a single PSF corresponding to the image center.

Attention was focused on observations with single-conjugate AO systems which exhibit very strong anisoplanatism compared to uncompensated imaging (on long time scales) and multi-conjugate or ground-level AO. A large set of AO long-exposure PSFs were simulated analytically using the PAOLA package [13]. The central point of this analytical approach is the calculation of the residual phase spatial power spectrum from which the optical transfer function and subsequently the PSF can be easily obtained. This calculation is done via filtering of the pure atmospheric phase spectrum with a set of filters responsible for: AO fitting error, temporal error, wavefront measurement error and, most importantly in our case, the anisoplanatism error. The advantage of this analytical method over traditional Monte-Carlo simulations is a huge reduction of the computational cost (few minutes instead of several hours or days).

The simulations were carried out for the 3.5-m SOR telescope located at a site of rather bad seeing in New Mexico. Therefore, for all the turbulence vertical profiles explored as part of this project a common value of $1.2''$ for seeing was adopted. (Seeing angle is defined as the full-width-at-half-maximum of the long-exposure PSF taken through turbulence at 500 nm wavelength). With Nyquist-sampled PSFs (two pixels per λ/D) a 256×256 pixel FOV covers $7.5''$. As test object we used the schematic image of the Hubble Space Telescope (HST) depicted in Fig. 6. It can be easily calculated that HST covers around $5''$ when observed from the ground. The test image was therefore padded with zeros to simulate a $7.5''$ FOV. Magnitude of the guide star (natural or laser-generated) was set to 10 in the visible, overall transmission from guide star (GS) to detector was set to 15%. Zenith angle was set to 30°. Wavelength of the observations was set to 1 μm. The AO system has many parameters and majority of them are outside the scope and interest of this work. Most important parameter is the density of actuators on the deformable mirror and simulations followed the current design of SOR AO system with 24×24 actuators. The other parameters were either taken from SOR AO design documents [14] or optimized to obtain the highest Strehl ratio on axis.

Most importantly, the influence of turbulence profile on PSF variability in the FOV was examined by testing various refractive index structure constant C_n^2 vertical distributions found in the literature. In brief: pupil-plane turbulence yields very isoplanatic images while concentration of strong turbulence higher up leads to severe anisoplanatism. Here, we show results obtained with two real turbulence profiles which had been obtained in the course of site testing in the context of the European Extremely Large Telescope project [15]. One profile ("atmosphere 1") has strong ground-level turbulence and produces little anisoplanatism. The contrary is true for the second profile which we call "atmosphere 2" here. Properties of both profiles are given in Table 2.

In the simulations, firstly a GS image was generated and put either at the center of the FOV (for stellar field images) or in the top right corner of the FOV for images of artificial satellites, as would be the case in laser-guide-star AO. Subsequently, a loop over positions generated a PSF for every location in the FOV according to its field angle and orientation with respect to the GS. These PSFs were then stored for subsequent convolution/deconvolution.

Images of satellites and stellar fields were obtained in dissimilar fashion. For satellites, all possible eigen-PSFs that can be computed from previous PSFs were used to convolve a ground-truth image, weighted with the corresponding set of coefficients, according to Equation (3). Since the complete set of eigenvectors and coefficients was used without reducing the dimensionality, the solution at each location of the FOV is the same as the one that would have been obtained with an individual PSF at such location. Object flux was set to 8.8×10^7 photons for both satellite models considered in this work (HST and the "fan" satellite).

Table 2. Atmospheric models. The strongest atmospheric layers are framed in red.

Atmosphere 1			**Atmosphere 2**		
Height $[m]$	**Fractional C_n^2**	**Windspeed $[m/s]$**	**Height $[m]$**	**Fractional C_n^2**	**Windspeed $[m/s]$**
0	0.335	12.1	47	0.410	5.0
600	0.223	8.6	140	0.010	4.6
1200	0.112	18.6	281	0.030	3.9
2500	0.090	12.4	562	0.060	3.5
5000	0.080	8.0	1125	0.010	3.9
9000	0.052	33.7	2250	0.080	6.4
11500	0.045	23.2	4500	0.140	12.7
12800	0.034	22.2	9000	0.140	27.2
14500	0.019	8.0	18000	0.130	9.0
18500	0.011	10.0	-	-	-

For stellar fields, a loop over thousand stars executed two tasks for each object: choice of position (random distribution; uniform over FOV) and choice of brightness. For the latter, the so-called initial mass function was employed to first pick randomly a mass for a star (exponential distribution with varying exponents according to [16]). Then, mass-luminosity relation for main-sequence stars was used to arrive at luminosity of the star. Brightness of GS was selected to be the luminosity cut-off, i.e. GS was always the brightest object in the FOV. Finally, an empty image border with no stars was used to avoid the wrap-around effect.

Leftmost panel in Fig. 4 shows the left half of a stellar field. The image is corrupted with shot and readout noise of $10e^-$ RMS. The GS is placed close to the mid-right side of this half-FOV, i.e., at the center of the entire image. Subsequent panels in Fig. 4 show the result of using algorithm [7] over this image for different number of PCs. Notice how the stars are better resolved as the number of PCs increases. In particular, it is interesting to stress that with only the first 2 PCs, corresponding to the diffraction core of the PSFs (see Fig. 2), there are still residuals along the diagonal and horizontal directions as we move further out from the GS position. This effect is corrected once the information corresponding to the elongation is included by means of PCs number 3 and 4. PC number 3 includes variations along the diagonal direction while PC number 4 corrects the horizontal-vertical aberrations.

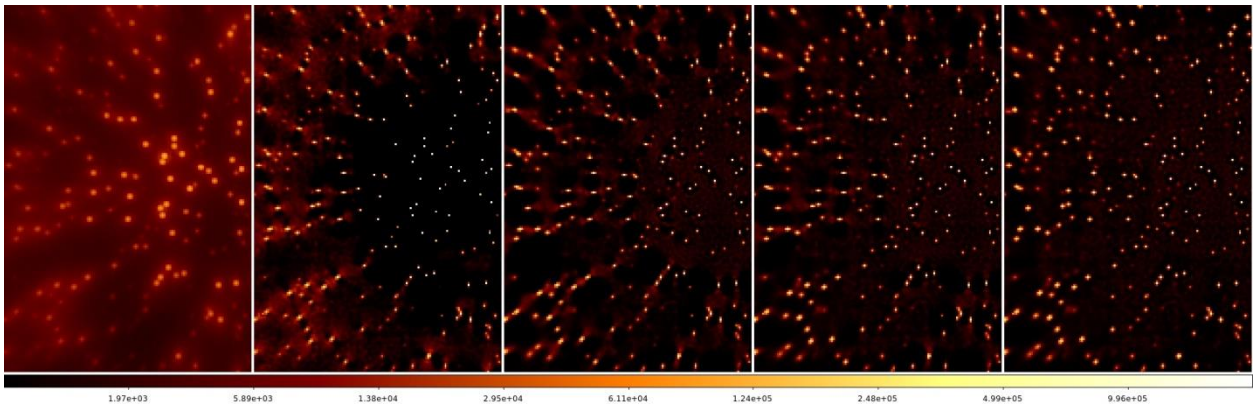

Fig. 4. Leftmost panel: input blurred and noisy image for atmosphere number 2. Data is corrupted with shot and readout noise of $10e^-$ RMS. From left to right: different reconstructions using [7] for 1 (69.75% of accumulated variance), 2 (86.48%), 3 (91.39%) and 4 (95.79%) PCs, respectively. The algorithm was stopped at the same number of iterations in all 4 cases. Images are represented in log scale. GS is close to the mid-right side of the image.

The addition of a larger number of PCs helps the reconstruction process. Algorithms like RL are very efficient in the first iterations; however, the lack of regularization produces the undesired effect of noise amplification when the

number of iterations is excessive. In other words, the level of reconstruction, i.e., the amount of noise in the final image, must be controlled when the number of iterations increases. Fig. 5 shows how the number of PCs and the number of iterations are somehow correlated. Two coaxial circles of stars with the same luminosity are simulated. The GS is placed beyond the upper right corner so the star closer to the lower left corner is the one most affected by anisoplanatism. It is noticeable that the more PCs are included in the reconstruction process the more "protected" the final image is against the noise amplification. The reader is invited to observe in the bottom row of Fig. 5 that the residuals over the inner circle are more symmetric and less affected by noise when 10 PCs are used with respect to only 5 PCs. Still, there are almost no differences between using 5 or 10 PCs when one observes the residuals over the outer circle. When 30 PCs are used all sources are better reconstructed over both circles.

Stronger anisoplanatism requires more PCs to represent the PSF. At the same time, more blurry and more elongated PSFs will need more iterations to concentrate all the light in their corresponding location and will be proportionally more affected by noise than those PSFs closer to the GS. Therefore, an increase in the number of deconvolution iterations at a certain location in the FOV will require an increase in the number of PCs that represent the PSFs there.

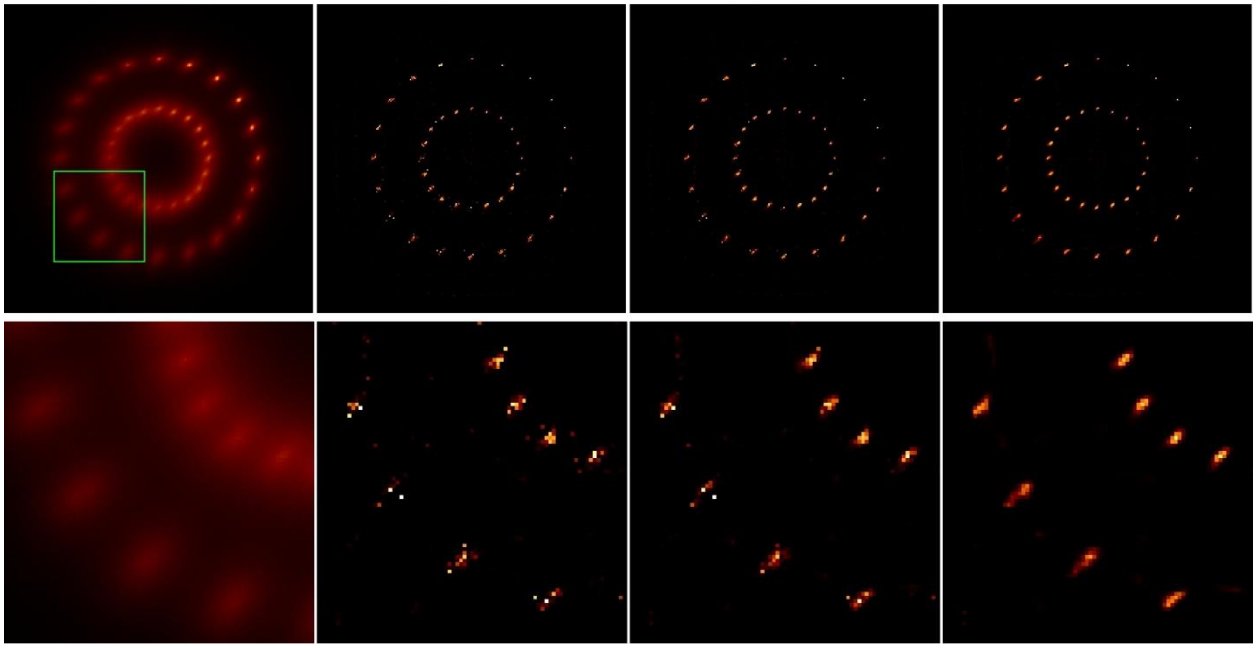

Fig. 5. Top row, leftmost panel: input blurred and noisy image for atmosphere number 2. Data is corrupted with shot and readout noise of $10e^-$ RMS. All sources have the same brightness. GS is placed beyond the upper right corner. Image is represented in asinh scale from 0 to $50E3$. From left to right: different reconstructions using [7] for: 5 (96.78% of accumulated variance), 10 (99.51%), and 30 (99.97%) PCs, respectively. The algorithm was stopped at the same number of iterations in all three cases. Images are represented in asinh scale from 0 to $500E3$. Bottom row: zoom-in view corresponding to the green square in the leftmost panel of the top row.

Figures 6 to 8 show reconstructions of artificial satellites using methods [12] (Equation 8) and [9] (Equation 9). The set of PSFs used to blur the original image is the same as in Fig. 5. Images have been corrupted only with readout noise of $10e^-$ RMS. Fig. 6 shows how the methods making use of static PSFs are not able to produce good reconstructions in those parts of the object that are far from the position where the reference PSF is located. Results obtained with the algorithms adapted to the use of PCs are significantly better (Fig. 6, rightmost panels). However, in Fig. 7 one can observe that different parts of the satellites would need different numbers of iterations to completely homogenize the reconstruction quality or consider a more robust restoration method. Regions closer to the GS (upper right corner) suffer from noise amplification whereas regions further out are still smooth.

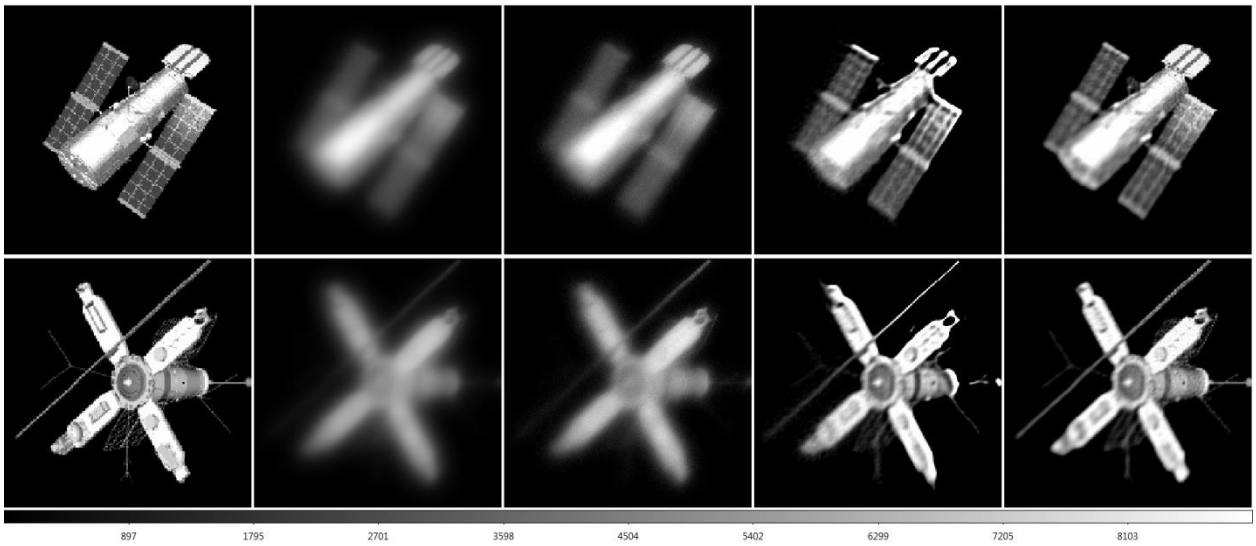

Fig. 6. Leftmost column: ground-truth image. Second column: blurred and noisy image for atmosphere number 2. Data is corrupted with only readout noise of $10e^-$ RMS. Guide star is placed beyond the upper right corner. Field of view is 256×256 pixels. Third column: reconstruction using Landweber method [12] with reference PSF at position $(255,255)$. Fourth column: reconstruction using Landweber method with reference PSF at position $(127,127)$. Rightmost column: reconstruction using Landweber method with 50 PCs (99.996% of accumulated variance). All reconstructions are stopped at $1E4$ iterations.

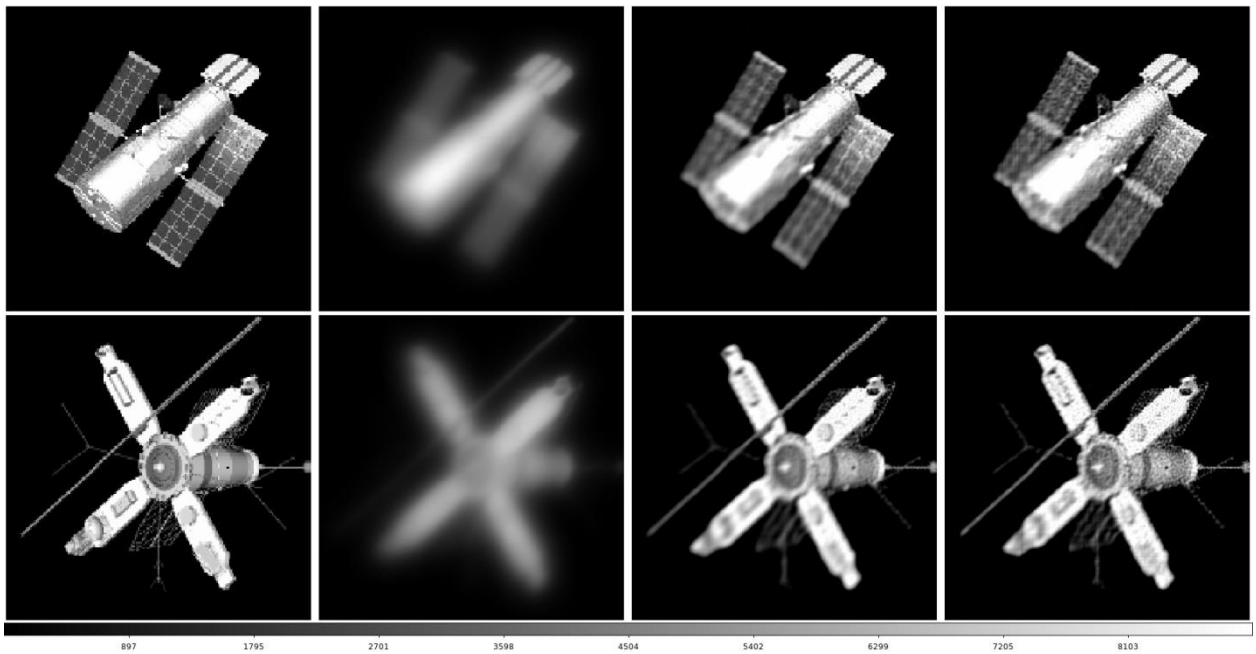

Fig. 7. Leftmost column: ground-truth image. Second column: blurred and noisy image for atmosphere number 2. Data is corrupted with only readout noise of $10e^-$ RMS. Guide star is placed beyond the upper right corner. Field of view is 256×256 pixels. Third column: reconstruction using Landweber method [12] with 50 PCs (99.996% of accumulated variance), and $1E4$ iterations. Rightmost column: $4E4$ iterations.

Method [9] makes use of the wavelet transform (WT) to filter out the noise. In this work we have used the translation-invariant Haar pyramid although other possibilities are also valid, such as the 2-D dual tree complex WT or a combination of both. The values of the regularization parameter υ and the threshold level in the wavelet domain are needed to be set. Reference [9] proposes some optimal values for certain levels of noise and a certain set of PSFs that are different from the ones considered in this work, thus resulting in different PC decompositions. Fig. 8 shows

the results for different values of the regularization parameter in Equation (9), obtaining sharper reconstructions with increasing values of υ. Nevertheless, we found that values larger than 9 started to produce visible artifacts (see Fig. 8, rightmost panels).

Results in Fig. 8 show that algorithm [9] allows to control noise amplification better than [12] in regions close to the GS but also stops the enhancement of further-out regions too soon, thus stressing the need of finding a method that allows to homogenize the quality of the final solution across the entire FOV.

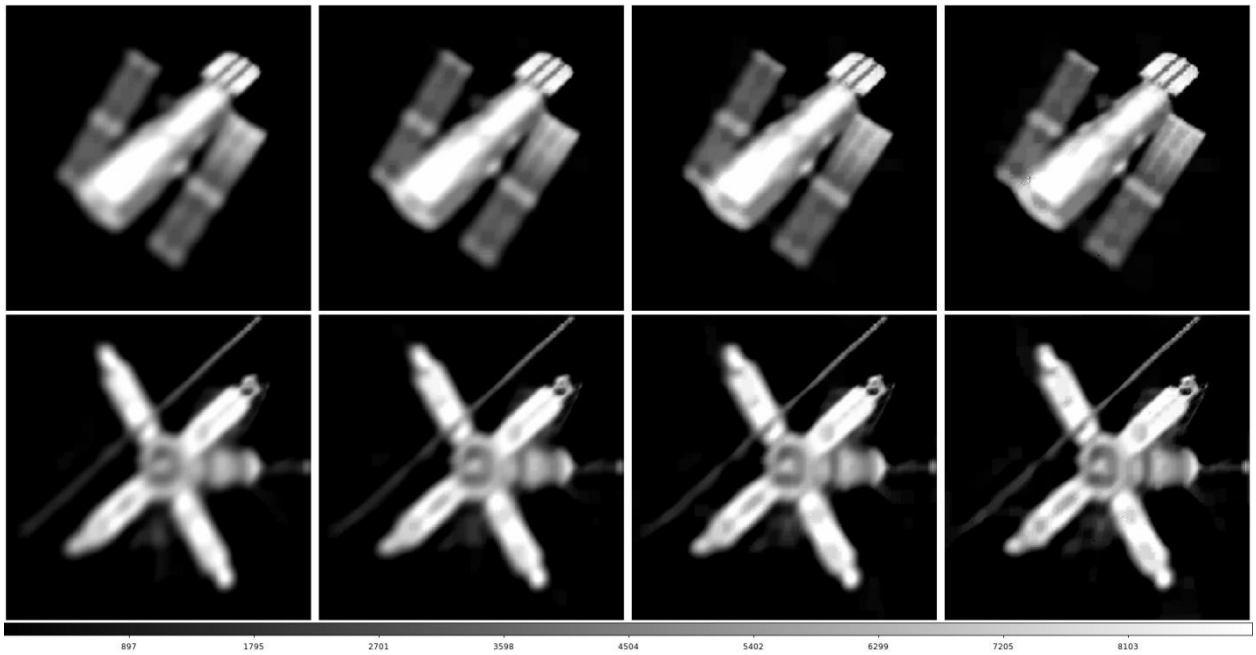

Fig. 8. Reconstructions using Miraut method [9] with 50 PCs (99.996% of accumulated variance). From left to right: regularization parameter υ equal to 1.04, 2.09, 4.17 and 8.35, respectively.

5. CONCLUSIONS AND FUTURE WORK

In this work we have shown the applicability of spatially-varying image deconvolution based on principal component analysis to anisoplanatic PSFs for single-conjugate AO systems. These techniques have been applied to both stellar fields and extended objects. We showed that the increase of the number of eigen-PSFs in the deconvolution process helps to control noise amplification. However, to homogenize the quality of the reconstructions, without compromising the achieved level of resolution, it is necessary to add regularization terms which include PC rigorously.

Results shown in this work are based on the unrealistic assumption of having a perfect knowledge of all the PSFs involved in the image degradation. Therefore, for a 256×256 pixel FOV a total number of 65536 kernels is required. This also means having a perfect knowledge of all the coefficients, at each location, which weight the importance of the corresponding PCs across the FOV.

Even in the case of observations of stellar fields, where PSFs could be extracted at a few locations within the FOV from isolated stars, the lack of knowledge of the PSF at most of the pixels would necessitate estimation of the PC coefficients wherever the PSF is unknown. Reference [5] uses 5th order polynomial interpolation to model the spatial variation of such coefficients using the known coefficients as fixed points. However, the authors state that higher-order polynomial can worsen the fidelity between the data and the proposed model. Different interpolation methods have been proposed for describing the spatial variation of the PC coefficients. Reference [11] concludes

that Kriging gives the most reliable interpolation but this conclusion was based on very specific type of astronomical data, namely weak lensing surveys.

Furthermore, PCA has been performed over noise-free PSFs. Shot and readout noise was introduced in the simulations after the ground-truth image was degraded. In real situations, extracted PSFs will be corrupted by the unavoidable presence of noise and, in the case of satellites, for which a myopic/blind deconvolution algorithm can be used to compute the degradation kernel in specific locations, the deduced PSFs will be affected by the uncertainties associated with that deconvolution process. Departures from the ground-truth PSFs will translate to different PC decompositions, i.e., different types of eigen-PSFs and coefficients, and a different number of eigen-PSFs to properly describe the same amount of PSF variability. Such differences must be studied in order to take into account their effect in this reconstruction problem.

Finally, introduction of PCs into the RL algorithm is straightforward: one only needs to substitute the PSF by a weighted sum of eigen-PSFs. However, the application of PCs in more complicated approaches, e.g., into the Bayesian framework, can be mathematically intractable. The authors of reference [9] had to apply an approximation to include PCs in a simple regularized inverse filter. The design of myopic/blind deconvolution approaches with PCA is the next natural step in spatially-varying imaging.

ACKNOWLEDGEMENTS

This material is based upon work supported by the Air Force Office of Scientific Research, Air Force Material Command, USAF under Award No. FA9550-14-1-0244 DEF, Ministerio de Ciencia e Innovación under Contract TIN2013-43880-R and the European Regional Development Fund (FEDER). We also extend our gratitude to Dr. Javier Portilla (IO-CSIC).

6. REFERENCES

[1] Hirsch, M.S., *Blind Deconvolution in Scientific Imaging & Computational Photography*, Thesis, Tübingen, 2011.
[2] Nagy, J.G. and O'Leary, D.P., Fast iterative image restoration with a spatially-varying PSF, *Proceedings of SPIE*, Vol. 3162, 388-399, 1997.
[3] Baena-Gallé, R. and Gladysz, S., Estimation of Differential Photometry in Adaptive Optics Observations with a Wavelet-based Maximum Likelihood Estimator, *PASP*, Vol. 123, 865-878, 2011.
[4] Refregier, A., Shapelets - I., A method for image analysis, *MNRAS*, Vol. 338, 35-47, 2003.
[5] Jee, M.J. et al., Principal component analysis of the time- and position-dependent PSF of the advanced camera for surveys, *PASP*, Vol. 119, 1403-1419, 2007.
[6] Popkin, T., Cavallaro, A. and Hands, D., Accurate and efficient method for smoothly space-variant Gaussian blurring, *IEEE Transactions on image processing*, Vol. 19, 1362-1370, 2010.
[7] Lauer, T.R., Deconvolution with a spatially-variant PSF, *Proceedings of SPIE*, Vol. 4847, 167-173, 2002.
[8] Flicker, R.C. and Rigaut, F.J., Anisoplanatic deconvolution of adaptive optics images, *JOSA A*, Vol. 22, 504-513, 2005.
[9] Miraut, D. and Portilla, J., Efficient shift-variant image restoration using deformable filtering (part I), *Eurasip journal on advances in signal processing*, Vol. 2012:100, 2012.
[10] Press, W.H. et al., *Numerical recipes*, Cambridge Univ. Press, Cambridge, 1992.
[11] Bergé, J. et al., On point spread function modelling: towards optimal interpolation, *MNRAS*, Vol. 419, 2356-2368, 2012.
[12] Landweber, L., An iteration formula for Fredholm integral equations of the first kind. *Amer. J. Math*. 73, 615–624, 1951.
[13] Jolissaint, L., Véran, J.-P. and Conan, R., Analytical modeling of adaptive optics: foundations of the phase spatial power spectrum approach, *JOSA A*, Vol. 23, 382-394, 2006.
[14] Johnson, R., Montera, D., Schneeberger, T. and Spinhirne, J., A New Sodium Guidestar Adaptive Optics System for the Starfire Optical Range 3.5m Telescope, in Frontiers in Optics 2009/Laser Science XXV, OSA Optics & Photonics Technical Digest, OSA Technical Digest (CD), 2009.

[15] http://www.eso.org/sci/facilities/eelt/science/drm/tech_data/ao/
[16] Kroupa, P., On the variation of the initial mass function, *MNRAS*, Vol. 322, 231-246, 2001.